RSC Advances

ROYAL SOCIETY OF CHEMISTRY

www.rsc.org/advances

Graphical abstract

The formaldehyde sensing properties of SnO_2 nanorods gas sensor are improved by compositing with Zn_2SnO_4.

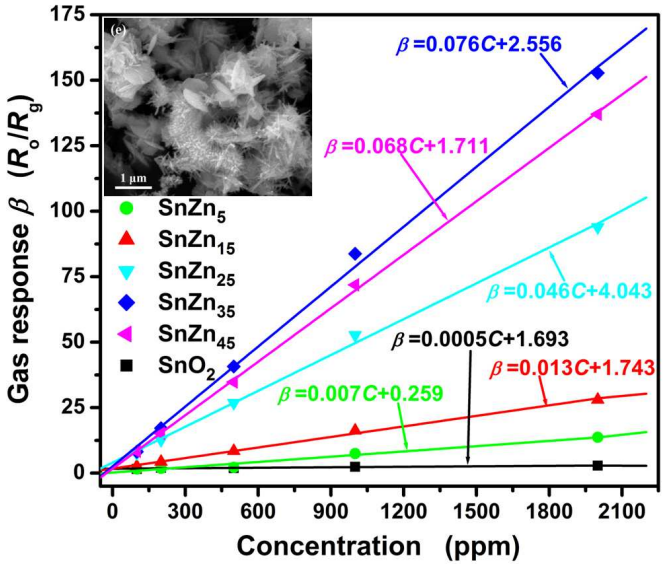

Enhanced formaldehyde sensing properties of SnO_2 nanorods coupled with Zn_2SnO_4

Xuechun Xiao [a], Xinxin Xing [a], Bingqian Han [a], Dongyang Deng [a], Xiaoyan Cai [a], Yude Wang [a,b,*]

a *School of Physical Science and Technology, Yunnan University, 650091 Kunming, People's Republic of China*

b *Yunnan Province Key Lab of Mico-Nano Materials and Technology*, *Yunnan University, 650091 Kunming, People's Republic of China*

E-mail: ydwang@ynu.edu.cn

* To whom correspondence should be addressed. Tel: 86-871-65031410, Fax: 86-871-65031410. E-mail: ydwang@ynu.edu.cn

Abstract

Ternary oxide Zn_2SnO_4 was introduced to rod-like nanostructured SnO_2 gas sensor for formaldehyde detection by a facile one-step hydrothermal synthesis. The effects of Zn_2SnO_4 additive on the structure, morphology and gas-sensing property of SnO_2 were investigated in this study. It was confirmed that control of the Zn amounts in the precursor solution was effective in realizing well-developed one- and two-dimensional coexisting structured SnO_2-Zn_2SnO_4 (SnZn) nanocomposites. Gas sensing properties of the resulting SnZn composites to HCHO vapor were tested. The results showed that the presence of Zn_2SnO_4 species in SnO_2 powders could effectively enhance electrical conductivity, reduce optimal operating temperature and improve gas response of the sensors. The composite exhibited the highest response towards HCHO in the case of 35 at.% Zn_2SnO_4 nanoplates coupling with hierarchical branched structures of SnO_2 nanorods ($SnZn_{35}$) at a relatively lower operating temperature of 162 $^{\circ}$C. The good gas-sensing performance of $SnZn_{35}$ composite can be ascribed to the smaller particle size, the larger surface area and the more absorbed O_x^- species, which all were favorable for gas diffusion and sensing reactions. This work renders great potential in the fabrication of gas sensor using binary-ternary oxide composite, which can be further applied in indoor pollution detection.

Keywords: SnO_2-Zn_2SnO_4 composite; 1D-2D hybrid structure; Gas sensor; Formaldehyde

1. Introduction

As an important industrial chemical, formaldehyde is utilized in the manufacturing of building boards, plywood and lacquer materials [1,2]. Moreover, it is an intermediate in consumer products, such as detergents and soaps, and also used in pharmacology and medicine because of its sterilization property. However, the investigated results showed that formaldehyde could cause many damages to the human body because it is a volatile and deleterious compound [3,4]. The most common symptoms related to formaldehyde exposure include irritation of the eyes, nose and throat, which occurs at air concentrations of about 0.4~1 parts per million (ppm). Higher concentration of formaldehyde even could cause damage to the central nervous system as well as the blood and immune system [5]. Therefore, effective methods to monitor formaldehyde have been demanded for atmospheric environmental measurement and control. The fabrication of gas sensors is thought to be a desirable means for monitoring the gases. Our present investigation mainly deals with the detection of formaldehyde.

For large requirement of formaldehyde sensor, a considerable amount of current research activities has been devoted to the development of formaldehyde sensor based on metal oxide semiconductors including SnO_2 [6], ZnO [7], NiO [8], TiO_2 [9], WO_3 [10] and In_2O_3 [11], and so on. Amongst them, SnO_2 has been proven to be the most attractive metal oxide for gas sensor application and extensively applied to detect various gaseous molecules like C_2H_5OH, *i*-C_4H_{10}, NO, CO, NO_2 [12]. Nevertheless, conventional and simplex SnO_2, suffering from lack of selectivity and durability, usually could not meet the requirements to qualify for high-performance indoor formaldehyde gas sensors. In order to

improve the gas sensing properties of SnO_2, several design features have been developed, including metal element (e.g., Zn and Sb) adulteration [13,14], noble metal (e.g., Pd and Ag) surface modification [15,16], multicomponent combination (e.g., SnO_2-ZnO and SnO_2-NiO) [17,18], structural and architectural innovation [6] and so forth. Nowadays, the addition of one or more oxide semiconductors to SnO_2 has been devoted to improve the sensing characteristics in order to monitor formaldehyde gas more effectively [19,20]. On the other hand, as an important ternary semiconductor oxide, zinc stannate (Zn_2SnO_4) has many promising applications in various advanced technologies such as gas sensor, Li-ion battery and photocatalyst because of its high chemical sensitivity, low visible absorption and excellent optical electronic properties [21]. SnO_2-Zn_2SnO_4 nanocomposite based sensors, which were applied to detect CO and ethanol gas, respectively, demonstrated better gas-sensitive properties than pure SnO_2 and Zn_2SnO_4 at a relatively higher operating temperature around 300 $^{\circ}$C [22,23]. However, to our knowledge, so far there is no report on the detection of formaldehyde vapor over nanostructured SnO_2-Zn_2SnO_4 composites in a relatively low operating temperature.

In this paper, we report a simple hydrothermal process for the fabrication of SnO_2 nanorods-Zn_2SnO_4 nanoplates composite gas-sensing materials and their improved formaldehyde sensing properties at low operating temperature. The structure, morphology and composition of the as-synthesized samples were characterized by X-ray diffraction analysis (XRD), scanning electron microscopy (SEM), transmission electron microscopy (TEM) and X-ray photoelectron spectroscopy (XPS). The performances of the sensor have been discussed according to the surface chemical reactions between the gas phase and the

semiconductor. The experimental results show that the sensor offers advantages in terms of the simple design and the facile preparation and the good gas response for formaldehyde.

2. Experimental details

2.1 Preparation of SnO_2-Zn_2SnO_4 composites

All the chemical reagents used in the experiments were obtained from commercial sources as guaranteed-grade reagents and used without further purification. A simple hydrothermal route was employed to synthesize the gas sensitive composite materials.

In a typical synthetic experiment, 0.525 g $SnCl_4 \cdot 5H_2O$ and a certain amount of $Zn(CH_3COO)_2 \cdot 2H_2O$ with the different Zn amounts in the range of 5.0~45 at.% were respectively dissolved in a mixed solution of 30 mL absolute alcohol and 30 mL deionized water under continuous magnetic stirring. As soon as 0.72 g NaOH was introduced, the reaction solution became cloudy accompanying with large of white precipitates. After magnetic stirring for 5 min and ultrasonic dispersing for 15 min successively, the mixture was poured into a Teflon cup (80 mL) in a stainless autoclave and then heated at 180 °C for 15 h. After the completion of reaction, the autoclave was taken out from the incubator and cool down spontaneously to the room temperature. The white precipitates were collected after centrifugation, washing and dried in air at 60 °C for 12 h. The composites with the Zn/(Sn + Zn) ratio ranging from 5~45 at.% were referred to as $SnZn_x$, x = 5, 15, 25, 35 and 45, respectively. Pure SnO_2 was also synthesized by same procedure.

2.2 Characterization of as-prepared powders

X-Ray diffraction (XRD, Rigaku D/MAX-3B powder diffractometer) with copper target and Kα radiation (λ = 1.54056 Å) was used for the phase identification, where the

diffracted X-ray intensities were recorded in the range from 20° to 80° (2θ) in step of 0.02°. The mean crystallite sizes (R_x) were measured from XRD peaks at a scan rate of 2°/min based on the Scherrer's equation: $R_x = 0.9\lambda/(B\cos\theta)$, where λ is the wavelength of X-ray, θ is the diffraction angle, and B is the true half-peak width. Scanning electron microscopy (SEM) characterization was performed on XL30ESEM-TMP microscope operating at 15 kV. Transmission electron microscopy (TEM) measurement was performed on a Zeiss EM 912Ω instrument at an acceleration voltage of 120 kV. The samples for TEM were prepared by dispersing the final samples in deionized water, and this dispersing was then dropped on carbon-copper grids covered by an amorphous carbon film. To prevent agglomeration of nanostructures the copper grid was placed on a filter paper at the bottom of a Petri dish. X-ray photoelectron spectroscopy (XPS) was carried out at room temperature in ESCALAB 250 system. During XPS analysis, an Al Kα X-ray beam was adopted as the excitation source and the vacuum pressure of the instrument chamber was 1×10^{-7} Pa.

2.3. Preparation of gas sensor

The sensors of indirect heating were fabricated according to the literature [14]. The mixed material used as a sensitive body was fabricated on an alumina tube with Au electrodes and platinum wires. A Ni-Cr alloy wire crossing the alumina tube was used as a resistor. This resistor ensured both substrate heating and temperature control. The thickness of the sensitive body based on SnO_2-Zn_2SnO_4 composite was approximately 0.5 mm after the body was calcinated at 450 °C for 2 h in air (Fig S1 in Supplementary Material). In order to improve their stability and repeatability, the gas sensors were aged at an operating temperature of 150 °C for 150 h in air. The export signal of the sensor was measured by

using a conventional circuit mentioned in our previous works [24], in which the element was connected with an external resistor in series at a circuit voltage of 5 V. The gas response β was defined as the ratio of the electrical resistance in air (R_o) to that in gas (R_g) (Fig S2 in Supplementary Material). All of the values of sensing performances are tested under a 30 % relative humidity. In addition, the response time was defined as the time required for the gas response reaching 90% of the final equilibrium value after a test gas was injected, and the recovery time was the time needed for gas response decreasing its 90% after the gas sensor was exposed in air again.

3. Results and discussion

3.1. XRD analysis

Fig. 1 shows the XRD pattern of the products with a series of Zn/(Sn + Zn) molar ratio prepared in alcohol-water mixture solution under hydrothermal condition. As shown in Fig. 1(c), one can see that all the diffraction peaks can be indexed to the rutile structure of SnO_2 with tetragonal lattice parameters a = 4.738 Å and c = 3.187 Å, which is consistent with the standard data file (JCPDS No. 41-1445). The relative intensity of the peaks deviates from those of the standard data and the strongest peak corresponds to the (101) plane of rutile structure, suggest the anisotropic growth of the SnO_2 crystals. From Fig. 1(d), the XRD pattern of the final product reveals well-developed reflections of SnO_2, without any indication of crystalline byproducts such as ZnO, Zn_2SnO_4 or $ZnSnO_3$. It implies that the Zn doping most probably occurs by substituting stannum atoms in the crystal structure. When the Zn content is up to 15 at.% in the reaction system, it can be clearly seen from Fig. 1(e)-(h) that all diffraction peaks can be assigned to the tetragonal phase of SnO_2 coexisting

with the cubic phase of Zn_2SnO_4 with the lattice constant a = 8.657 Å (JCPDS No. 24-1470). Theoretically, since the ion radius of Zn^{2+} (0.74 Å) is larger than that of Sn^{4+} (0.71 Å), the (101) peaks of $SnZn_x$ composites should move to smaller angle slightly when compared to that of pure SnO_2 (2θ = 33.93º) obtained at the same condition if the Zn doping occurs by incorporating into the SnO_2 lattice. From Fig. 1, it can be seen that the (101) peaks of $SnZn_x$ composites slightly shift to a low angle ($2\theta \approx 33.86$º). The lattice constants of the samples are presented in Table 1. The values of lattice constants of $SnZn_x$ composites are slightly increased when compared to that of ICDD values of SnO_2 (a = 4.738 Å, c = 3.187 Å). Meanwhile, compared with the pure SnO_2, the diffraction peaks of the composites are obviously broadened, indicating the small crystallite size, which are also proved by the calculated results in Table 1. In addition, as the Zn content increased, the stronger Zn_2SnO_4 peaks as well as the weaker SnO_2 peaks are found in the composite systems, which symptomatize an interaction between the components of the composites.

The process of SnO_2-Zn_2SnO_4 formation can be schematized by the following set of equations [25]:

$$Sn^{4+} + 6OH^- = Sn(OH)_6^{2-} \quad (1)$$

$$Zn^{2+} + 4OH^- = Zn(OH)_4^{2-} \quad (2)$$

$$Zn^{2+} + Sn(OH)_6^{2-} = ZnSn(OH)_6 \quad (3)$$

$$Zn(OH)_4^{2-} + Sn(OH)_6^{2-} = ZnSn(OH)_6 + 4OH^- \quad (4)$$

$$Sn(OH)_6^{2-} = SnO_2 + 2H_2O + 2OH^- \quad (5)$$

$$ZnSn(OH)_6 + Zn(OH)_4^{2-} = Zn_2SnO_4 + 4H_2O + 2OH^- \quad (6)$$

Prior to the hydrothermal process, $Sn(OH)_6^{2-}$ and $Zn(OH)_4^{2-}$ precipitates are

formed using NaOH as the alkaline mineralizer (Eq. (1) and (2)). During the hydrothermal stage, $ZnSn(OH)_6$ crystal nucleus are generated from the $Sn(OH)_6^{2-}$ and $Zn(OH)_4^{2-}$ precursors (Eq. (3) and (4)). Afterwards, SnO_2 and Zn_2SnO_4 crystals would be produced through the direct hydrolysis of $Sn(OH)_6^{2-}$ (Eq. (5)), and the reaction between $ZnSn(OH)_6$ and superfluous $Zn(OH)_4^{2-}$ (Eq. (6)), respectively.

3.2. SEM and TEM analysis

SEM analysis for the pure SnO_2 and $SnZn_x$ composites synthesized under the same hydrothermal conditions were carried out to show the morphological evolution of the as-prepared products as the Zn^{2+} concentration in the reaction system increased. From Fig. 2(a), the morphology of the pure SnO_2 look like flower clusters formed by tetragonal prisms with square cross-section ends, and the nanorods are seen to be up to 1 μm in length and 100 nm in diameter. When 5 at.% Zn ions (molar ratio) are doped into the SnO_2 nanorods, irregular bush-like aggregates are congregated by more quantity of rods comparing with that of the undoped sample. As can be seen in Fig. 2(b), the formed one-dimensional rod-like nanostructures have an average diameter of 60 nm and a length of several hundred of nanometers, which are smaller than pure nanorods in size. After the introduction of more quantity of Zn^{2+} (15 at.%), cube-shaped Zn_2SnO_4 with uniform size (~300 nm in edge length) are obtained and SnO_2 clusters assembled from a number of short nanorods with the length about 200 nm dispersed around the nanocubes as revealed in Fig. 2(c). We know that the orthorhombic Zn_2SnO_4 has a cubic spinel structure, and this crystal nature is in favor of the formation of cubic morphology under certain conditions auto-generated by hydrothermal treatment [21]. As the concentration of Zn goes from 25 to

45 at.% (Fig. 2(d)-(f)), the obtained SnO_2 nanorods and Zn_2SnO_4 nanocubes are changing sequentially both in size and shape. The nanorods in the products are conical, not prism-shaped, and the average diameter of them is less than 50 nm. Particularly, only a small number of nanorods are observed in Fig. 2(f). Compared with that of sample $SnZn_{15}$, $SnZn_{25}$ and $SnZn_{35}$, the rods of $SnZn_{45}$ are obviously decrescent, in which the average lengths of the ultra-small nanorods are merely 50 nm. On the other hand, as a transitory stage, Fig. 2(d) shows that the nanocubes appear to split into some nubbly aggregates of irregular plates with increasing Zn content from $SnZn_{15}$ to $SnZn_{25}$ composites, and the morphology of Zn_2SnO_4 completely turns to be that of nanoplates with irregular petaloid shape when the molar ratio of Zn/(Sn + Zn) is equal or greater than 0.35. The nanoplates are about 10 nm in thickness and hundreds of nanometers in planar size as shown in Fig. 2(e) and (f). In summary, it is clear that the more Zn content in the reaction systems, the more Zn_2SnO_4 nanoplates whereas the fewer SnO_2 nanorods in the resulting composites. Also, the size and morphology of the products can be tunable by changing the dosage of Zn^{2+}. XRD study showed that Zn ions could suppress the nucleation and growth of SnO_2, resulting in spatial distribution of Zn related nanoparticles. Although slight modification in the shape of the rods is observed with the coupling of composites, overall anisotropic growth of SnO_2 is maintained.

Investigations by TEM provide insight into the morphological and structural features of the SnO_2-Zn_2SnO_4 nanostructured composite. Fig. 3 shows the representative TEM images of sample $SnZn_{35}$. Fig. 3(a) clearly depicts the co-existence of slightly-aggregated 1D nanorods and 2D nanoplates, which are in accordance with the results of the SEM. Closer

observation reveals that radial secondary SnO_2 branches emanated from the backbone nanorods with pointed ends are obtained through the introduction of 35 at.% Zn^{2+}. The backbone nanocones have length and diameter (bottom) the range of 100~500 μm and 30~50 nm, whereas the secondary branches have length and diameter ranging from 20~200 nm and 10~30 nm, respectively. The image also demonstrates that the Zn_2SnO_4 nanoplates are very thin. Fig. 3(b) displays a cluster of branched SnO_2 nanorods, where the rod-like backbones grow from a junction point with random orientation, and correspondingly, branches grow on the side walls of backbones with different radial angles. The growth of hierarchical branched structures can be attributed to the tiny mismatch of lattice spacings derived from the regulation of moderate concentrated Sn-Zn binary solution into interstitial voids between backbone SnO_2 nanorods [26]. HRTEM image in Fig. 3(c) gives the spacing between the lattice planes along the width of the nanorod of 0.267 nm, and is well consistent with (101) planes of the rutile SnO_2, indicating that the SnO_2 nanorods grew along the [112] direction. The corresponding selected-area electron diffraction (SAED) pattern of an ensemble of one- and two-dimensional hybrid nanocomposites is shown in Fig. 3(d). The spotted diffraction rings from the inside to the outside can be indexed to the (110), (101), (200), (211) and (220) planes of rutile SnO_2, as well as the (311) and (440) planes of spinel Zn_2SnO_4, respectively. These indexed patterns are in good accordance with the XRD reflections described above. It seems that their gas-sensing effect may benefit by much more specific surface area from the coupling of branched nanorods and ultra-thin nanoplates.

3.3. XPS analysis

XPS was further used to probe the surface chemical compositions and chemical

oxidation state of the as-prepared nanocomposites. Fig. 4(A) and (B) show high-resolution XPS spectra of Sn3d and Zn2p of pure SnO_2 and $SnZn_x$ composites, respectively. Sn3d spectra of pure SnO_2 (Fig. 4(A)) exhibit two peaks of $Sn3d_{5/2}$ and $Sn3d_{3/2}$ at 486.3 and 494.7 eV with better symmetry, which are assigned to the lattice tin in SnO_2. The distance between these two peaks is 8.4 eV, being in good agreement with the energy splitting reported for SnO_2. The values correspond to the 3d binding energy of Sn(IV) ions (indexed Standard ESCA Spectra of the Elements and Line Energy Information, F Co., USA). In the regions of Sn3d, there remains an apparent distinction between pure and composite materials. About 0.1~0.4 eV chemical shift of Sn3d have been observed after Zn component introduced in the SnO_2, which may be explained by the presence of many Zn cations in SnO_2 lattices, creating an oxygen-rich surface layer on the composites [27]. On the other hand, the patterns observed in Fig. 4(B) are due to the spin orbit splitting of Zn2p level giving rise to $Zn2p_{3/2}$ and $Zn2p_{1/2}$ levels with energy separation of 22.9 eV. Binding energies of $Zn2p_{3/2}$ and $Zn2p_{1/2}$ levels for the three samples are perceived at 1019.6 ± 0.5 eV and 1042.3 ± 0.3 eV, respectively. The values are close to the reported literatures [28] and confirm that Zn is present mainly in 2+ oxidation state. Obviously, the relative intensity of Zn2p in $SnZn_{35}$ is much larger than that in $SnZn_{15}$ and $SnZn_5$ composites, suggesting the enhancement of Zn incorporation and the increase of Zn_2SnO_4 production.

Also, the Gauss fitting curves of O1s spectra of sample SnO_2, $SnZn_{15}$ and $SnZn_{35}$ are present in Fig. 5 to identify the oxygen chemical states of the obtained gas sensitive materials. Three deconvoluted peaks centered at ca. 530.0, 531.5, and 532.7 eV can be identified, which indicate that there are three sorts oxygen in the surface, the lattice oxygen

($O_{lattice}$), the adsorbed oxygen (O_x^-) and bound oxygen ($O_{adsorbates}$), respectively. The peak at 530.0 eV can be ascribed to O^{2-} ion which is characteristics of oxygen in metal oxide such as Sn-O and Sn-O-Zn under fully oxidized stoichiometric conditions [29]. The highest binding energy of 532.7 eV is classified as the loosely bound oxygen on the surface of the sample, which are chemisorbed or dissociated oxygen or OH species [30]. The binding energy of 531.5 eV results from the absorbed O_x^- ions (O^- and O_2^- ions) in the oxygen deficient regions within the matrix of SnO_2 caused by oxygen vacancy (V_O), oxygen interstitial (O_i), and oxygen antisite (O_{Sn}) [31,32]. The lattice oxygen could not be interacted with the reducing gas, and unable to affect the formation of the main charge-carrier holes in n-type semiconductor. However, the absorbed O_x^- ions are reactable with the gas and then enhance the holes concentration [33]. Therefore, the increasing of adsorbed oxygen ions contributes to gas sensitivity.

3.4. Sensing properties

To evaluate the potential applicability in gas sensor for VOCs, we investigated fundamental gas sensing properties of the as-synthesized $SnZn_x$ composites. It is well accepted that the sensing response of gas sensors is greatly influenced by the working temperature and the amount of additives [34]. Therefore, in order to obtain the best response and keep the stability of a sensor, choosing an optimal operating temperature is undoubtedly necessary. The gas sensing properties of the pure SnO_2 and $SnZn_x$ composites towards 1000 ppm of formaldehyde vapor were investigated in detail with working temperature from145 to 214 ˚C in dry air. Fig. 6 depicts the relation between the response and the operating temperature for the sensors. One can see that the operating temperature

has a great influence on the response. As expected, the response first gradually increases and then decreases with increasing the operating temperature. This behavior can be explained in analogy with the mechanism of gas adsorption and desorption on semiconducting oxides [35]. However, it can be seen that the $SnZn_x$ composites based sensors show excellent gas-sensing characteristics to HCHO gas than that of SnO_2 nanorods, in which $SnZn_{35}$ composite exhibits the highest response to HCHO at a relative low temperature of 162 ˚C. At the operating temperature of 145 and 195 ˚C to formaldehyde vapor of 1000 ppm, the corresponding gas responses of $SnZn_{35}$ composite are 37.8 and 28.0, respectively. The effect of operating temperature is pronounced, and the gas response reaches a maximum of 83.8 when the temperature is adjusted to 162 ˚C. The gas response increases more than 190 ^{o}C, which is not in agreement with the reported literatures and not clear. However, the optimal operating temperature value is ascertained using two requirements: one is that has high gas response; another is that has lower temperature. The low operating temperature is very important in practical applications because it will have low energy consumption. Therefore, this temperature has been chosen for monitoring different HCHO concentrations [14].

As shown in Fig. 7, the gas responses of the pure SnO_2 and $SnZn_x$ composites based sensors operated at 162 ˚C show good dependence on the HCHO gas concentrations. The straight lines of the samples are the calibration curves and the experimental data are fitted as: $\beta = mC_{gas} + k$, where m is the gas response coefficient, C_{gas} is the concentration of HCHO gas, and k is a constant. The correlative coefficients R^2 are more than 0.99 indicating a good linear dependence. The results show a remarkable increase in response to

HCHO gas compared with the pure SnO_2 and other $SnZn_x$ composites. Fig. 7 shows that the system of SnO_2 nanorods combining with 35 at.% Zn_2SnO_4 nanoplates exhibits the gas responses toward 100, 200, 500, 1000, and 2000 ppm ammonia are 8.1, 17.7, 40.9, 83.8, and 152.9, respectively. From the obtained straight line, we calculated m=0.076±0.002 for $SnZn_{35}$ composite. According to the equation, the low detection limit toward formaldehyde is calculated to be 1 ppm. On the contrary, the gas response of SnO_2 nanorods is only 2.4, which is just 1/35 of the $SnZn_{35}$ composite. Moreover, the gas response of the $SnZn_{35}$ composite is also much higher than that of other $SnZn_x$ (x=5, 15, 25 and 45) composites at a concentration of 1000 ppm, further demonstrating its superior gas-sensing property. According to the definition of response/recovery time, the response and recovery time are calculated to be 35 s and 78 s, respectively.

Since thermal energy may cause the electrons to transfer from the valence band (or donor levels) to the conduction band and at the same time increases the mobility of the charge carriers [36], the relationship between resistances of the $SnZn_x$ based sensors and operating temperature illustrates a decreasing resistance with the increasing temperature in the testing range of 145~214 °C (not shown here). When the temperature is low, the electrons on valence band do not possess enough energy to jump to the conduction band, causing the low conductivity. As the temperature rises, the electrons on valence band gain enough energy to jump into the conduction band and result in the conductivity increase. Fig. 6 has shown the optimal working temperature of 214 °C for pure SnO_2, 195 °C for $SnZn_5$ and $SnZn_{15}$, and 162 °C for $SnZn_{25}$, $SnZn_{35}$ and $SnZn_{45}$ composites, respectively, demonstrating the declining optimal operating temperature with Zn incorporation into the

SnO_2 gas sensing materials. The resistance in air (R_o) of the sensors operated at 162 ˚C as well as their corresponding maximum response (β) to 2000 ppm formaldehyde vapor as a function of Zn content, is displayed in Fig. 8. The electrical conductivity and gas response of pure SnO_2 nanorods are much smaller than that of $SnZn_x$ composites. The resistance values of the $SnZn_x$ composites decrease with the mole fraction of Zn ions increased from 5 at.% to 35 at.% but increase when the content of Zn exceeds 35 at.%. An opposite tendency is observed when it comes to gas response values. These changes may mostly be ascribed to the increasing amount of the resistive Zn_2SnO_4 phase, which can reduce the operating temperature effectively. As a result of the increase in the charge carriers, the increasing electrical conductivity of $SnZn_{35}$ composite may also contribute to its gas response improved, owing to the addition of moderate amount of Zn_2SnO_4 [22].

The gas response measured at this temperature also showed a good dependence on the gas concentration. As shown in Fig. 9, the sensor exhibits as high as 153 of gas response at 2000 ppm formaldehyde concentration, while the sensitivities to volatile organic compound (VOC) vapors, such as alcohol, methanol, isopropanol and acetone, are 67.1, 41.6, 29.6 and 21.2, respectively. On the other hand, the gas responses of the low detection toward gases at 100 ppm are 8.1, 2.3, 3.6, 5.5, and 4.5 for formaldehyde, acetone, isopropanol, alcohol, and methanol, respectively. Alcohol is one of the most interfering gases to formaldehyde detection. Much work has been done to find new materials sensitive to formaldehyde, but their gas response to alcohol is higher than formaldehyde [37]. In our work, this nanostructured SnO_2-Zn_2SnO_4 composite sensor showed good selectivity to alcohol, methanol, isopropanol and acetone.

In practical application, the long-term stability of gas sensors has attached much attention for which determined the reliability of gas sensors and the length of service. To verify the stability of the sensor, the gas response evolutions in about 5 weeks were tested under the different conditions (100, 200, 500, and 1000 ppm HCHO). The 21-days-later response is slightly changed ±16.1%, ±6.1%, ±3.4%, and ±1.4% for 100, 200, 500, and 1000 ppm HCHO gas, respectively, illustrating good stability of the sensor (Fig. 10). The stability mechanism is more complicated and further work is to be done to get a definite understanding.

As we know, gas-sensing mechanism is not fully understood and subject to ongoing discussion [38]. The commonly accepted gas-sensing mechanism for n-type semiconducting metal oxides like SnO_2 and Zn_2SnO_4 involves an adsorption-oxidation-desorption process in which chemisorbed oxygen plays a crucial role [39]. The HCHO sensing process can be described as below [6]:

$$O_{2gas} \leftrightarrow O_{2ads} \leftrightarrow O^-_{2ads} \leftrightarrow 2O^-_{ads} \leftrightarrow 2O^{2-}_{ads} \quad (7)$$

$$HCHO_{ads} + 2O^-_{ads} \rightarrow CO_2 + H_2O(g) + 2e^- \quad (8)$$

$$HCHO_{ads} + 2O^{2-}_{ads} \rightarrow CO_2 + H_2O(g) + 4e^- \quad (9)$$

In air condition, oxygen is adsorbed on its surface and then ionized into O^- or O_2^- via attracting electrons from SnO_2 or Zn_2SnO_4 semiconductor (Eq. (7)). Once the sensor exposed to HCHO gas, HCHO molecules can be fully absorbed or interact with the adsorbed oxygen according to the reactions depicted in Eq. (8) and (9). These reactions can enhance the free electron concentration, and consequently, the resistance of the sensor decreases to produce a sensor response (Fig S3 in Supplementary Material).

After coupling with 35 at.% plate-like nanostructured Zn_2SnO_4, the particle size of the produced $SnZn_{35}$ composite is smaller than that of pure SnO_2 and other $SnZn_x$ (x=5, 15, 25 and 45) composites as shown in Table S1. TEM investigation of the $SnZn_{35}$ composite has presented the SnO_2 nanorods with hierarchical branched architecture coexisting with ultra-thin Zn_2SnO_4 nanoplates, which has a large surface area. Both the smaller particle size and the larger surface area are favorable for the gas-sensing performance. The XPS result (Fig. 5(c)) illustrates more absorbed O_x^- species (O^- and O_2^- ions) in the $SnZn_{35}$ composite, which is argued to contribute to the higher gas-sensing performance. Oxygen vacancies have been argued to favor dissociative adsorption of oxygen on the semiconductor surface [40] and are also reported to facilitate the isopropanol gas adsorption and charge transfer from the surface to the adsorbate on the surface of SnO_2 porous powders which in turn enhanced the electrical responses [25]. Due to the formation of nanorod/nanoplate junctions, the 1D and 2D concomitant structured $SnZn_{35}$ composites possessed a unique morphology which shortens effectively the gas diffusion distance and provides highly accessible open channels and active surfaces for the target gas, favoring significantly the gas-sensing performance. Therefore, the $SnZn_{35}$ composite synthesized by hydrothermal synthesis here can exhibit an even improved gas-sensing property. Although the exact mechanism remains further clarified, the current study on the gas-sensing performance of the SnO_2-Zn_2SnO_4 composites may suggest that $SnZn_{35}$ composite is an effective material to HCHO gas detection. The future work will be done to have a detail understanding for the sensing mechanism of $SnZn_{35}$ composite.

4. Conclusions

The successful synthesis of SnO_2 nanorods and $SnZn_x$ nanocomposites with 1D-2D hybrid structure though hydrothermal process was presented. As-synthesized SnO_2 and $SnZn_x$ composites were characterized by XRD, SEM, TEM and XPS. The results revealed that $SnZn_{35}$ composite with small particle size, high specific surface area and high concentration of adsorbed oxygen was obtained. The resulting powders were used directly to prepare gas sensor devices by fabrication of the SnO_2 and $SnZn_x$ composites on the alumina tubes with Au electrodes and Pt wires. The sensor based on $SnZn_{35}$ composite showed good response and selectivity to HCHO gas at a low operating temperature of 162 $^{\circ}$C. Compared with the sensors fabricated with pure SnO_2 and other $SnZn_x$ (x=5, 15, 25 and 45) composites, the $SnZn_{35}$ composite sensor has about 1.2~152 times increase in gas response to HCHO. The experimental results indicate the potential of using $SnZn_{35}$ composite for formaldehyde gas sensing.

Acknowledgements

This work was supported by the National Natural Science Foundation of China (No. 51262029), the Key Project of the Department of Education of Yunnan Province (ZD2013006), Program for Excellent Young Talents, Yunnan University (XT412003), and Department of Science and Technology of Yunnan Province via the Key Project for the Science and Technology (Grant No. 2011FA001).

References

[1] Y. I. Korpan, M. V. Gonchar, A. A. Sibirny, C. Martelet, A. V. El'skaya, T. D. Gibson and A. P. Soldatkin, *Biosens. Bioelectron.* 2000, **15**, 77.

[2] K. W. Zhou, X. L. Ji, N. Zhang and X. R. Zhang, *Sens. Actuators B* 2006, **119**, 392.

[3] L. Feng, Y. J. Liu, X. D. Zhou and J. M. Hu, *J. Colloid. Interface Sci.* 2005, **284**, 378.

[4] Y. Herschkovitz, I. Eshkenazi, C. E. Campbell and J. Rishpon, *J. Electroanal. Chem.* 2000, **491**, 182.

[5] Y. X. Xia, Toxicity of Chemicals, *Shanghai: Shanghai Science and Technology, Literature Publishing House*, 1991.

[6] K. Xu, D. Zeng, S. Tian, S. Zhang and C. Xie, *Sens. Actuat. B* 2014, **190**, 585.

[7] F. C. Chung, Z. Zhu, P. Y. Luo, R. J. Wu and W. Li, *Sens. Actuat. B* 2014, **199**, 314.

[8] C. Y. Lee, C. M. Chiang, Y. H. Wang and R. H. Ma, *Sens. Actuat. B* 2007, **122**, 503.

[9] S. Lin, D. Li, J. Wu, X. Li and S. A. Akbar, *Sens. Actuat. B* 2011, **156**, 505.

[10] L. Deng, X. Ding, D. Zeng, S. Tian, H. Li and C. Xie, *Sens. Actuat. B* 2012, **163**, 260.

[11] W. Yang, P. Wan, X. Zhou, J. Hu, Y. Guan and L. Feng, *Sens. Actuat. B* 2014, **201**, 228.

[12] G. T. Ang, G. H. Toh, M. Z. A. Bakar, A. Z. Abdullah and M. R. Othman, *Process Saf. Environ.* 2011, **89**, 186.

[13] X. Ding, D. Zeng and C. Xie, *Sens. Actuat. B* 2010, **149**, 336.

[14] Y. D. Wang, I. Djerdj, M. Antonietti and B. Smarsly, *Small* 2008, **4**, 1656.

[15] M. Epifani, J. Arbiol, E. Pellicer, E. Comini, P. Siciliano, G. Faglia and J. R. Morante, *Cryst. Growth Des.* 2008, **8**, 1774.

[16] R. K. Joshi and F. E. Kruis, *Appl. Phys. Lett.* 2006, **89**, 153116.

[17] X. Song and L. Liu, *Sens. Actuat. A* 2009, **154**, 175.

[18] L. Liu, S. Li, L. Wang, C. Guo, Q. Dong and W. Li, *J. Am. Ceram. Soc.* 2011, **94**, 771.

[19] T. Chen, Q. J. Liu, Z. L. Zhou and Y. D. Wang, *Nanotechnology* 2008, **19**, 095506.

[20] P. Lv, Z. A. Tang, J.Yu, F. T. Zhang, G. F. Wei, Z. X. Huang and Y. Hu, *Sens. Actuat. B* 2008, **132**, 74.

[21] Y. Q. Jiang, C. X. He, R. Sun, Z. X. Xie and L. S. Zheng, *Mater. Chem. Phys.* 2012, **136**, 698.

[22] W. J. Moon, J. H. Yu and G. M. Choi, *Sens. Actuat. B* 2001, **80**, 21.

[23] Z. Lu and Y. Tang, *Mater. Chem. Phys.* 2005, **92**, 5.

[24] D. Hu, B. Q Han, R. Han, S. J. Deng, Y. Wang, Q. Li and Y. D. Wang, *New J. Chem.* 2014, **38**, 2443.

[25] G. Cheng, K. Wu, P. Zhao, Y. Cheng, X. He and K. Huang, *J. Cryst. Growth* 2007, **309**, 53.

[26] F. Zhao, X. Li, J. G. Zheng, X. Yang, F. Zhao, K. S. Wong, J. Wang, W. Lin, M. Wu and Q. Su, *Chem. Mater.* 2008, **20**, 1197.

[27] B. Mirkelamoglu and G. Karakas, *Appl. Catal. A: Gen.* 2006, **299**, 84.

[28] X. Y. Cai, D. Hu, S. J. Deng, B. Q. Han, Y. Wang, J. M. Wu and Y. D. Wang, *Sens. Actuat. B* 2014, 198, 402.

[29] Z. Ai, S. Lee, Y. Huang, W. Ho and L. Zhang, *J. Hazard. Mater.* 2010, **179**, 141.

[30] T. Kawabe, K. Tabata, E. Suzuki, Y. Yamaguchi and Y. Nagasawa, *J. Phys. Chem. B* 2001, **105**, 4239.

[31] L. G. Wang, Y. B. Ma, Y. Wang, S. M. Liu and Y. Q. Deng, *Catal. Commun.* 2011, **12**, 1458.

[32] M. Chen, Z. Wang, D. Han, F. Gu and G. Guo, *J. Phys. Chem. C* 2011, **115**, 12763.

[33] H. Aono, E. Traversa, M. Sakamoto and Y. Sadaoka, *Sens. Actuat. B* 2003, **94**, 132.

[34] G. Eranna, B. C. Joshi, D. P. Runthala and R. P. Gupta, *Crit. Rev. Solid State Mater. Sci.* 2004, **29**, 111.

[35] I. Djerdj, A. Haensch, D. Koziej, S. Pokhrel, N. Barsan, U. Weimar and M. Niederberger, *Chem. Mater.* 2009, **21**, 5375.

[36] W. Wen, J. M. Wu and Y. D. Wang, *Sens. Actuat. B* 2013, **184**, 78.

[37] D. Hu, B. Q. Han, S. J. Deng, Z. P. Feng, Y. Wang, J. Popovic, M. Nuskol, Y. D. Wang and I. Djerdj, *J. Phys. Chem. C* 2014, **118**, 9832.

[38] N. Barsan and U. Weimar, *J. Electroceram.* 2001, **7**, 143.

[39] A. Gurlo, *Chem. Phys. Chem.* 2006, **7**, 2041.

[40] Y. Yan, M. M. Al-Jassim and S. H. Wei, *Phys. Rev. B* 2005, **72**, 161207(R).

Captions of Figures

Figure 1 XRD patterns of as-prepared samples: SnO_2 (c) and $SnZn_x$ composites (d-h).

Figure 2 SEM images of as-prepared samples: (a) SnO_2, (b) $SnZn_5$, (c) $SnZn_{15}$, (d) $SnZn_{25}$, (e) $SnZn_{35}$ and (f) $SnZn_{45}$.

Figure 3 TEM images (a) and (b), HRTEM image (c), and SAED image (d) of $SnZn_{35}$ composite.

Figure 4 The high-resolution XPS spectra of sample SnO_2, $SnZn_5$, $SnZn_{15}$ and $SnZn_{35}$: (A) Sn3d, (B) Zn2p .

Figure 5 The high-resolution XPS spectra of O1s: (a) SnO_2, (b) $SnZn_{15}$, (c) $SnZn_{35}$.

Figure 6 Gas responses of the SnO_2 and $SnZn_x$ (x=5, 15, 25, 35 and 45, respectively) based sensor to formaldehyde gas of 1000 ppm at the different operating temperature.

Figure 7 Gas responses of the SnO_2 and $SnZn_x$ (x=5, 15, 25, 35 and 45, respectively) based sensors to different concentrations of formaldehyde gas at the operating temperature of 162 °C.

Figure 8 The resistance in air of the SnO_2 and $SnZn_x$ (x=5, 15, 25, 35 and 45, respectively) based sensors operated at 162 °C and their corresponding maximum response to 2000 ppm formaldehyde gas as a function of Zn content.

Figure 9 Gas response of $SnZn_{35}$ to the different concentrations of formaldehyde, alcohol, methanol, isopropanol and acetone at the operating temperature of 162 °C.

Figure 10 The gas response of $SnZn_{35}$ based sensor toward 100, 200, 500, and 1000 ppm

formaldehyde gas tested once a day for up to 21 days at operating temperature of 162 °C.

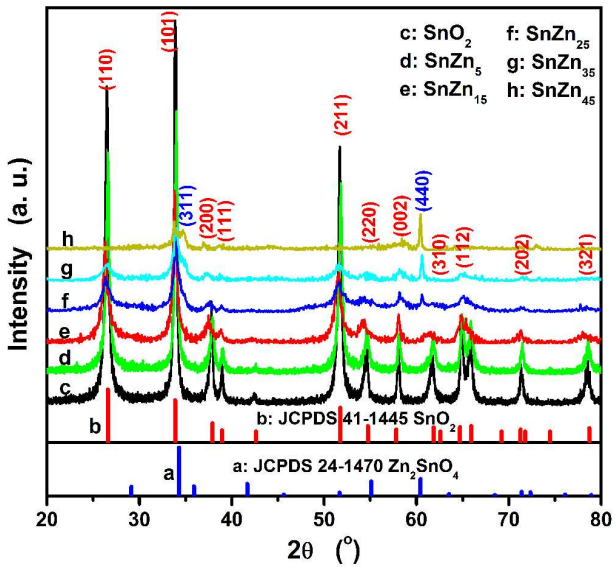

Figure 1

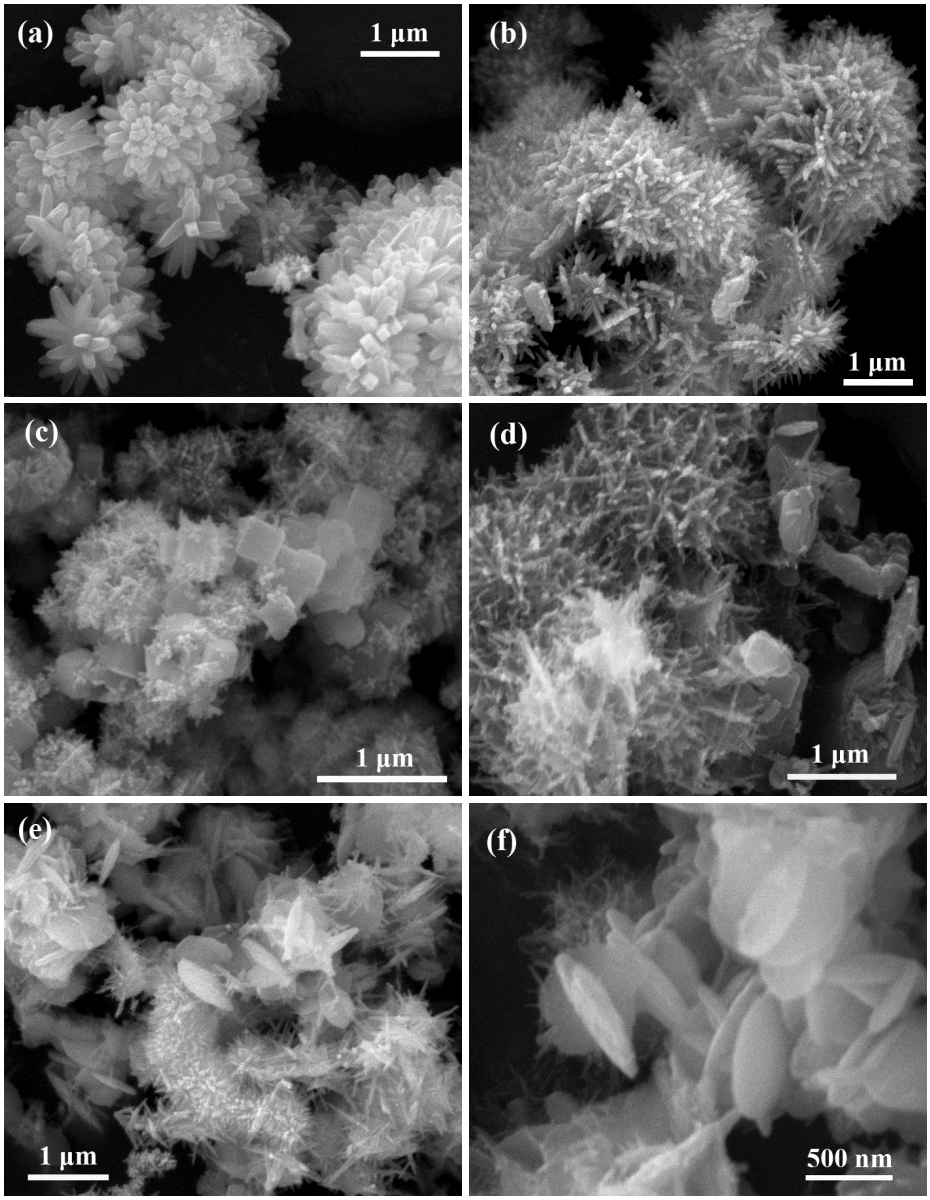

Figure 2

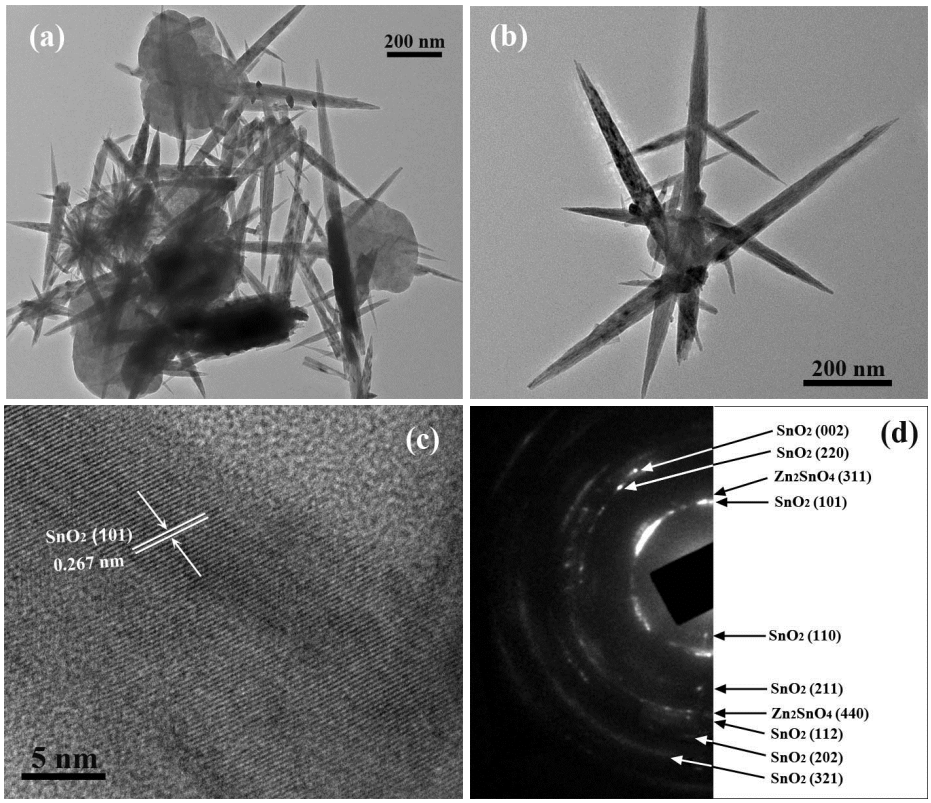

Figure 3

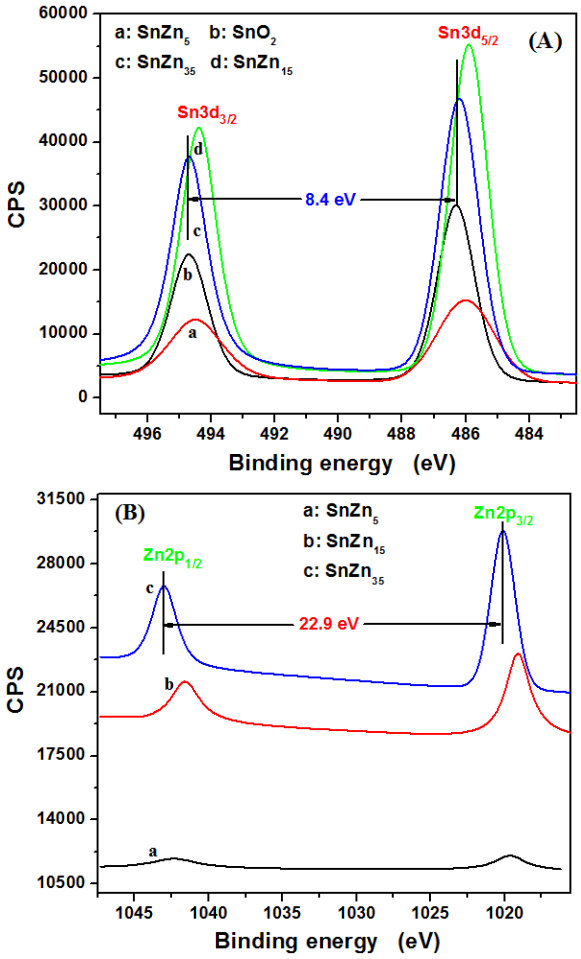

Figure 4

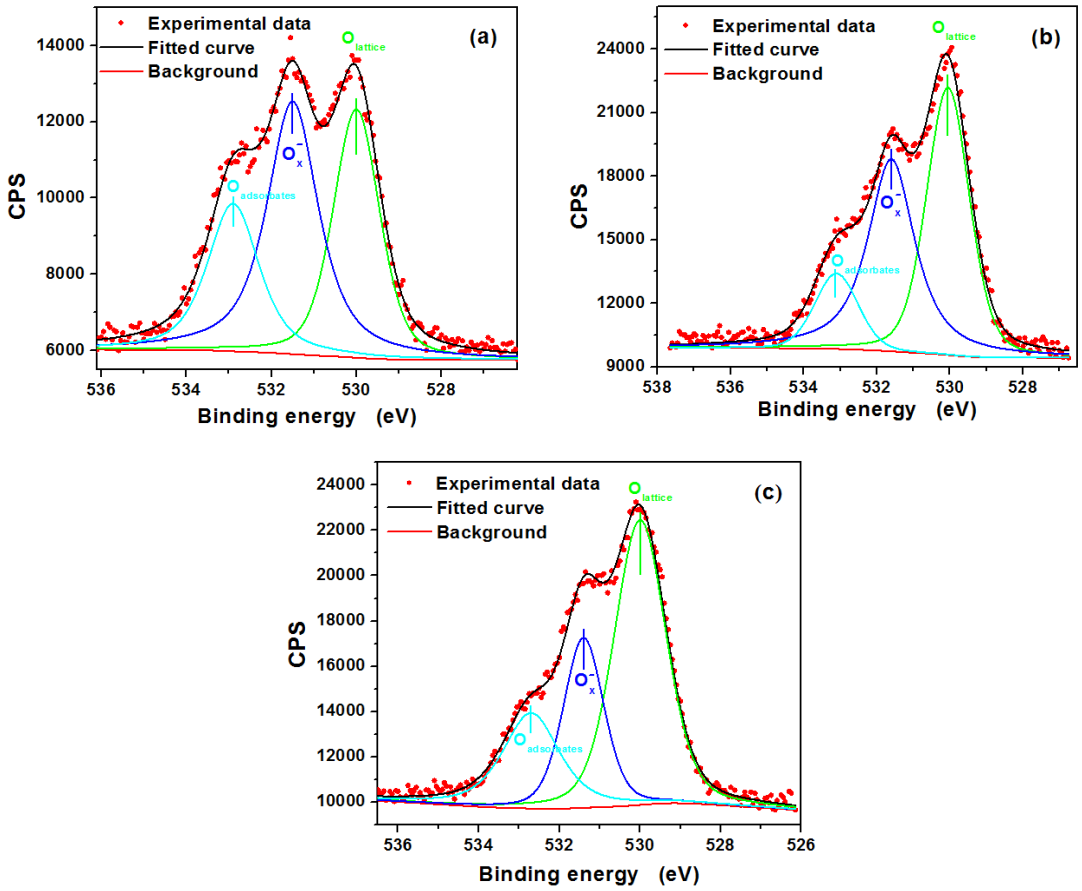

Figure 5

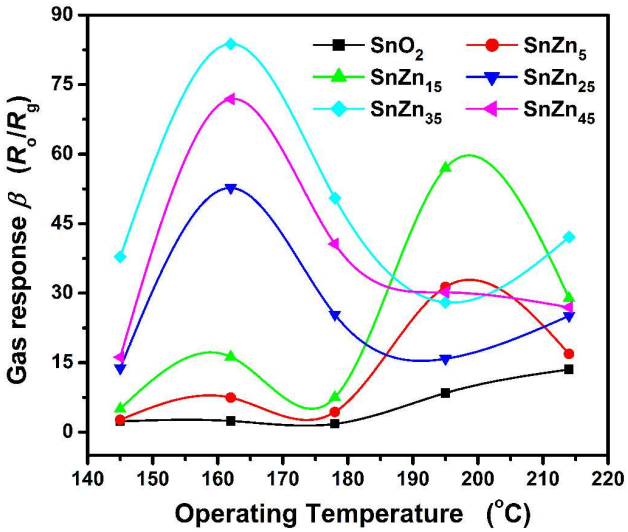

Figure 6

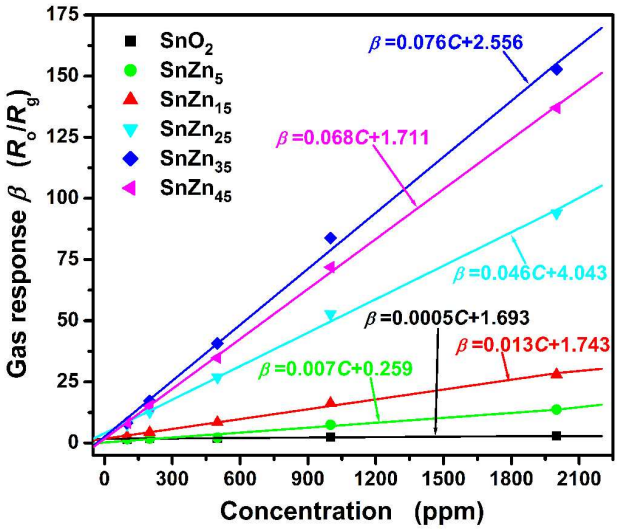

Figure 7

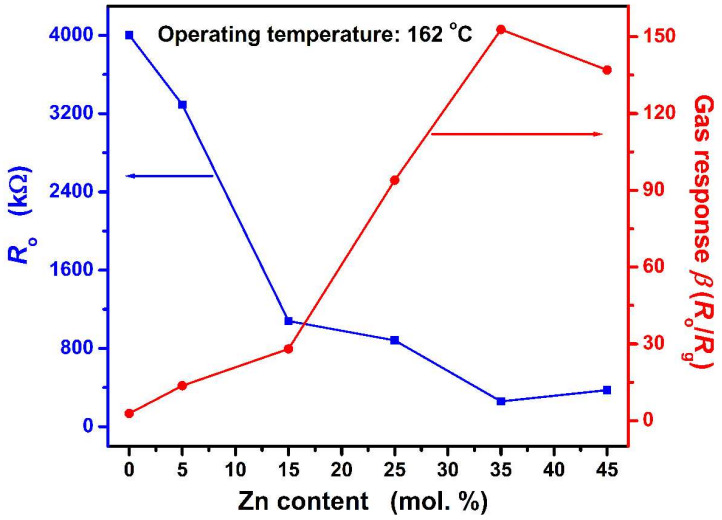

Figure 8

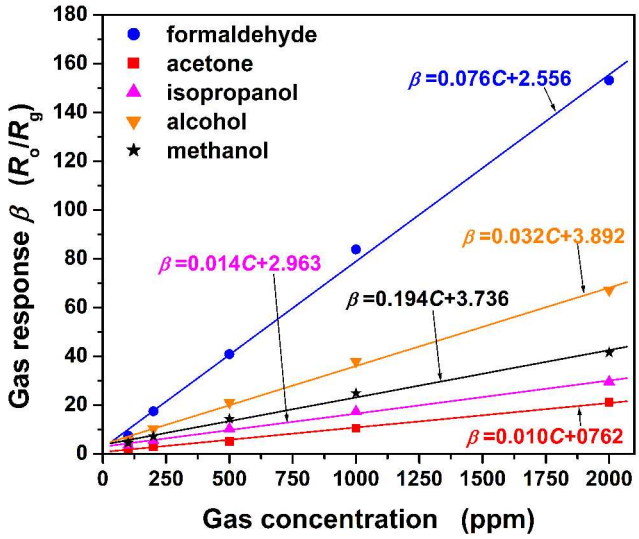

Figure 9

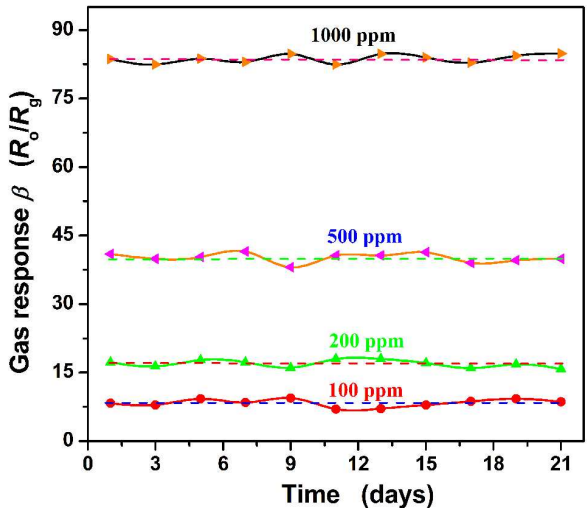

Figure 10